









High-resolution magnetic resonance and mass spectrometry imaging of the human larynx

Ayami Ohno Kishimoto¹  | Yo Kishimoto²  | Xudong Shi³  | Elizabeth B. Hutchinson⁴  | Hua Zhang⁵  | Yatao Shi⁵  | Gisele Oliveira^{6*} | Lingjun Li^{5,7}  | Nathan V. Welham³  | Ian J. Rowland⁸ 

¹Department of Diagnostic Radiology, Kyoto Katsura Hospital, Kyoto, Japan

²Department of Otolaryngology – Head and Neck Surgery, Graduate School of Medicine, Kyoto University, Kyoto, Japan

³Division of Otolaryngology – Head and Neck Surgery, Department of Surgery, University of Wisconsin-Madison, Madison, WI, USA

⁴Department of Biomedical Engineering, University of Arizona, Tucson, AZ, USA

⁵Division of Pharmaceutical Sciences, School of Pharmacy, University of Wisconsin-Madison, Madison, WI, USA

⁶Graduate Program in Speech-Language Pathology, Touro College, Brooklyn, NY, USA

⁷Department of Chemistry, University of Wisconsin-Madison, Madison, WI, USA

⁸Department of Entomology, University of Wisconsin-Madison, Madison, WI, USA

Correspondence

Nathan V. Welham, PhD, Division of Otolaryngology – Head and Neck Surgery, Department of Surgery, University of Wisconsin School of Medicine and Public Health, K4/723 CSC, 600 Highland Avenue, Madison, WI 53792, USA. Email: welham@surgery.wisc.edu

Funding information

National Institute of Diabetes and Digestive and Kidney Diseases, Grant/Award Number: R01 DK071801; National Institute of Mental Health, Grant/Award Number: R56 MH110215; National Institute of Dental and Craniofacial Research, Grant/Award Number: P50 DE026787; National Center for Research Resources, Grant/Award Number: S10 RR029531; National Institute on Deafness and Other Communication Disorders, Grant/Award Number: R01 DC004428, R01 DC010777 and R21 DC017836; National Cancer Institute, Grant/Award Number: P30 CA014520 and U01 CA231081

Abstract

High-resolution, noninvasive and nondestructive imaging of the subepithelial structures of the larynx would enhance microanatomic tissue assessment and clinical decision making; similarly, *in situ* molecular profiling of laryngeal tissue would enhance biomarker discovery and pathology readout. Towards these goals, we assessed the capabilities of high-resolution magnetic resonance imaging (MRI) and matrix-assisted laser desorption/ionisation-mass spectrometry (MALDI-MS) imaging of rarely reported paediatric and adult cadaveric larynges that contained pathologies. The donors were a 13-month-old male, a 10-year-old female with an infraglottic mucus retention cyst and a 74-year-old female with advanced polypoid degeneration and a mucus retention cyst. MR and molecular imaging data were corroborated using whole-organ histology. Our MR protocols imaged the larynges at 45–117 μm^2 in-plane resolution and capably resolved microanatomic structures that have not been previously reported radiographically—such as the vocal fold superficial lamina propria, vocal ligament and macula flavae; age-related tissue features—such as intramuscular fat deposition and cartilage ossification; and the lesions. Diffusion tensor imaging characterised differences in water diffusivity, primary tissue fibre orientation, and fractional anisotropy between the intrinsic laryngeal muscles, mucosae and lesions. MALDI-MS imaging revealed peptide signatures and putative protein assignments for the polypoid degeneration lesion and the N-glycan constituents of one mucus retention cyst. These imaging approaches have immediate application in experimental research and, with ongoing technology development, potential for future clinical application.

*Deceased.

Nathan V. Welham and Ian J. Rowland are Joint senior authors.

KEYWORDS

diffusion tensor imaging, glycomics, molecular imaging, mucus retention cyst, polypoid degeneration, proteomics, Reinke's oedema, vocal fold, whole-larynx histology

1 | INTRODUCTION

Imaging is an essential modality in the assessment of laryngeal anatomy and physiology. While the vocal fold epithelium is easily visualised on laryngoscopy, subepithelial integrity cannot be visualised directly and so is inferred from the mucosal surface contour and physiologic features of tissue oscillation during phonation (Rosen & Murry, 2000; Sulica, 2013). Clinically, in the absence of suspicion of papilloma, dysplasia or carcinoma, biopsy is typically deferred to avoid the risk of iatrogenic dysphonia, meaning that definitive pathological diagnosis of a presumed benign lesion is only obtained following surgical resection. Additional options for nondestructive vocal fold imaging would therefore enhance microanatomic assessment and—in clinical situations—provisional diagnosis, treatment planning and disease surveillance.

To date, experimental and early clinical efforts to advance the high-resolution imaging required for nondestructive subepithelial feature detection have focused on high-frequency ultrasound (Huang et al., 2007; Tamura et al., 2001, 2002; Walsh et al., 2008), optical coherence tomography (OCT; Armstrong et al., 2006; Burns et al., 2005, 2011; Jungheim et al., 2016; Klein et al., 2006; Maturo et al., 2012; Wong et al., 2005) and magnetic resonance imaging (MRI; Herrera et al., 2009; King et al., 2018; Kishimoto et al., 2016; Oleson et al., 2018, 2020). High-frequency ultrasound and OCT offer real-time imaging at 10–50 μm spatial resolution but require an imaging probe, have limited depth penetration and do not acquire images in broad anatomic context. MRI—which unlike X-ray and computerised tomography does not deliver ionising radiation—allows visualisation of whole tissues and organs (including collection of three-dimensional [3D] data), provides high contrast in connective tissues, and can be used to map molecular diffusion (Le Bihan et al., 2001). Prior MRI studies of vocal fold mucosa in dog, pig, rabbit, ferret and rat models have successfully characterised major anatomic landmarks, hydration status, surgical injuries, fibrosis and bioimplants at sub-50 μm resolution (Herrera et al., 2009; King et al., 2018; Kishimoto et al., 2016; Kolosova et al., 2020; Oleson et al., 2018, 2020).

Here, to expand on this previous work and explore translational potential in the human larynx, we conducted high-resolution MRI, including diffusion tensor imaging (DTI), of rarely reported cadaveric specimens: intact larynges from a 13-month-old infant, a 10-year-old child with an infraglottic mucus retention cyst and a 74-year-old adult with both advanced polypoid degeneration (Reinke's oedema) and a supraglottic mucus retention cyst. We corroborated our MRI findings with whole-larynx histology and *in situ* molecular characterisation of the laryngeal pathologies using matrix-assisted laser desorption/ionisation-mass spectrometry (MALDI-MS) imaging—a powerful molecular technology that enables *in situ* mapping of the spatial distribution of proteins, glycans and lipids within tissue

samples for biomarker discovery and enhanced pathological assessment (Calligaris et al., 2015; Caprioli et al., 1997; Eberlin et al., 2016; Stauber et al., 2010; Zhang et al., 2020).

2 | METHODS

2.1 | Cadaver tissue procurement and processing

Human larynges were obtained from three cadavers at autopsy with approval of the University of Wisconsin Health Sciences Institutional Review Board. The cadaveric donors were a 13-month-old male (cause of death, seizure disorder), 10-year-old female (cause of death, neuroblastoma) and 74-year-old female (cause of death, cardiopulmonary event). Larynges were obtained <24 h postmortem; the end-of-life airway status of the donors was unavailable. Each specimen was trimmed of oesophageal and hypopharyngeal tissue prior to imaging; the lateral thyroid cartilage (TC) laminae were removed from the 74-year-old specimen to accommodate the interior dimensions of the MRI volume coil. Samples were immersed in 4% paraformaldehyde (PFA) at 4°C for 7–10 days prior to image acquisition.

2.2 | MRI

MRI was performed in a 4.7 T instrument (Agilent Technologies) using a 210 mm bore magnet and standard volume coil. VnmrJ software (Agilent Technologies) was used for instrument control and data acquisition.

We began by acquiring non-contrast-enhanced (nCE) T1- and T2-weighted (T1W and T2W, respectively) images. Next, to reduce longitudinal relaxation time and evaluate its effect on tissue contrast, and because of its utility in our prior work with *ex vivo* rat larynges (Kishimoto et al., 2016), we repeated the T1W acquisition sequences following immersion in 5 mM gadobenate dimeglumine (Gd) contrast agent (MultiHance, Bracco Imaging) in 4% PFA for 10 days. All specimens were blotted to remove surface fluid and suspended in liquid perfluorocarbon prior to scanning.

Due to differences in laryngeal size and tissue composition, as well as pathologies in two of the three larynges, we used the following specimen-specific acquisition parameters: (a) T1W gradient echo (3D), 13-month-old specimen (repetition time/echo time [TR/TE], 20.6/6.5 ms; number of excitations [NEX], 24; flip angle [FA], 65°; field-of-view [FOV], 46 × 23 × 23 mm; matrix, 512 × 256 × 256; 90 μm^3 voxel resolution); (b) T1W spin echo (multi-slice), 13-month-old specimen (TR/TE, 1800/22 ms; NEX, 8; FOV, 23 × 23 mm; matrix, 512 × 512; 45 μm^2 in-plane voxel

resolution; 0.75 mm thickness; 41 slices); (c) T1W gradient echo (3D), 10-year-old specimen (TR/TE, 20.6/6.5 ms; NEX, 24; FA, 65°; FOV, 60 × 30 × 30 mm; matrix, 512 × 256 × 256; 117 μm^3 voxel resolution); (d) T1W spin echo (multi-slice), 10-year-old specimen (TR/TE, 3500/22 ms; NEX, 16; FOV, 30 × 30 mm; matrix, 512 × 512; 59 μm^2 in-plane voxel resolution; 1 mm thickness; 35 slices); (e) T2W spin echo (multi-slice), 10-year-old specimen (TR/TE, 6000/65 ms; NEX, 16; FOV, 32 × 32 mm; matrix, 512 × 512; 63 μm^2 in-plane voxel resolution; 1 mm thickness; 41 slices); (f) T1W gradient echo (3D), 74-year-old specimen (TR/TE, 20.6/6.5 ms, NEX, 24; FA, 65°; FOV, 60 × 30 × 30 mm; matrix, 512 × 256 × 256; 117 μm^3 voxel resolution); (g) T1W spin echo (multi-slice), 74-year-old specimen (TR/TE, 1800/22 ms; NEX, 12; FOV, 30 × 30 mm; matrix, 512 × 512; 59 μm^2 in-plane voxel resolution; 0.75 mm thickness; 55 slices).

Scan data were reviewed and analysed using ImageJ (Schneider et al., 2012). Volume rendering and measurements were performed using Horos 3.3.6 (Purview) and MIPAV 10.0.0 (National Institutes of Health).

2.3 | DTI

Larynges underwent a 10-day washout of Gd and PFA and rehydration in phosphate buffered saline prior to DTI; the instrument setup and specimen suspension in perfluorocarbon was as described above. Three unweighted and 30 diffusion-weighted images with b-value of 1000 s/mm^2 were acquired using a spin echo (multi-slice) pulse sequence (TE/TR, 1800/22 ms; NEX, 1). The spatial dimensions were as follows: 13-month-old and 10-year-old specimens (FOV, 30 × 30 mm; matrix, 128 × 128; 234 μm^2 in-plane voxel resolution; 1 mm thickness; 35 slices); 74-year-old specimen (FOV, 32 × 32 mm; matrix, 256 × 256; 125 μm^2 in-plane voxel resolution; 1 mm thickness; 35 slices).

DTI processing was performed offline using TORTOISE (Irfanoglu et al., 2017) to fit the diffusion tensor (DT) and generate maps for: (a) DT trace and mean diffusivity, to report the magnitude of water diffusivity; (b) fractional anisotropy, to report preferential directionality of tissue; and (c) directionally encoded colour (Pajevic & Pierpaoli, 1999), to show the primary orientation of tissue fibres. Quantitative region-of-interest analysis was performed for each intrinsic laryngeal muscle and each pathological lesion via manual tracing of the relevant DTI maps from each larynx using Functional Magnetic Resonance Imaging of the Brain Software Library (FSL) tools (Jenkinson et al., 2012).

2.4 | Histology

Specimens were refixed in 4% PFA for 3–7 days and processed for whole-larynx histology using a previously reported protocol (Wittekindt et al., 2006, 2008) with substitution of Cal-Ex (Thermo Fisher Scientific) for the decalcification step. Five- μm thick paraffin sections were cut in the axial plane; three serial sections per 25 were

stained with haematoxylin and eosin (H&E), Movat's pentachrome and alcian blue (pH 2.5), respectively. Stained sections were scanned using an Aperio CS2 digital slide scanner at 20 \times magnification (Leica Biosystems) and reviewed using Aperio ImageScope 12.1 (Leica Biosystems).

2.5 | MALDI-MS imaging

Tissue sections were annealed onto slides at 60°C for 30 min; deparaffinised by washing three times each in xylene, 100% ethanol, 95% ethanol and 70% ethanol; and heated in 20 mM citrate buffer (pH 6) at 95°C for 1 h to retrieve antigens.

To release N-glycans, 20 μl of 10 U/ μl PNGase F (Promega) dissolved in 380 μl of 15 mM ammonium bicarbonate buffer was sprayed onto tissue sections using a TM-Sprayer (HTX Technologies) with the following setup: flow rate of 10 $\mu\text{l}/\text{min}$, nozzle nitrogen gas pressure at 8 psi, nozzle temperature at 35°C, nozzle velocity of 800 mm/min, and tracking space of 2 mm. Following incubation in a humidified chamber at 37°C for 12 h, sections were sprayed with 40 mg/ml 2,5-dihydroxybenzoic acid (DHB) matrix in MeOH/H₂O/TFA (70:30:0.1 v/v/v) using a TM-Sprayer with the following setup: flow rate of 50 $\mu\text{l}/\text{min}$ for 20 passes, drying time of 30 s between each pass, nozzle nitrogen gas pressure at 10 psi, nozzle temperature at 80°C, tray temperature at 30°C, nozzle velocity of 1000 mm/min, and tracking space of 2 mm.

Prior to *in situ* peptide imaging, tissue sections were washed with 10 mM ammonium bicarbonate buffer to remove DHB matrix and released N-glycans, placed in a desiccator until dry, then sprayed with 100 ng/ μl trypsin gold (Promega) in 10 mM ammonium bicarbonate buffer using the same TM-Sprayer parameters described above for PNGase F deposition. After incubation in a humidified chamber at 37°C for 12 h, sections were sprayed with 40 mg/ml DHB in MeOH/H₂O/TFA (70:30:0.1 v/v/v) using the same TM-Sprayer parameters described above for matrix application.

MALDI-MS experiments were conducted using a MALDI-LTQ-Orbitrap XL mass spectrometer (Thermo Fisher Scientific) equipped with a 60 Hz 337 nm N₂ laser. MS data were collected in the positive ion mode with a mass-to-charge ratio (*m/z*) range of 100–3000, mass resolution of 60 K, raster step size of 75 μm and laser energy of 20 μJ . Xcalibur and ImageQuest (Thermo Fisher Scientific) were employed to perform data analysis; MSiReader (NC State University, Raleigh, NC) was used for image normalisation and ion map generation with 5 ppm mass error tolerance. N-glycan signal intensities were normalised to total ion count for the construction of N-glycan maps. The SwePep peptide database (Uppsala University, Uppsala, Sweden) was used for accurate mass matching of peptides with <10 ppm error tolerance.

N-glycan compositions were tentatively assigned by searching the UniCarbKB database (<https://www.glygen.org>); observed N-glycans were annotated using GlycoWorkbench (Damerell et al., 2012) with <10 ppm mass error tolerance; structures were drawn

according to the Symbol Nomenclature for Glycans (SNFG) format (Neelamegham et al., 2019).

To identify putative peptides/proteins associated with polypoid degeneration, peptide peaks unique to the lesion region were submitted to MS-FIT (<https://prospector.ucsf.edu/>) and protein assignments with MOlecular Weight SEarch (MOWSE) (Pappin et al., 1993; Perkins et al., 1999) scores of 75 and above were reported. The MOWSE score reflects the relative confidence of the protein assignment and is defined as $-\log_{10} P$ of the assignment occurring by chance.

3 | RESULTS

3.1 | Characterisation of paediatric and adult larynges at the glottis

We first assessed the ability of MRI to resolve key laryngeal substructures in the three specimens representing different ages and developmental stages (Figure 1; Videos S1–S3). Using contrast-enhanced (CE) T1W gradient and spin echo sequences and data acquisition at $45\text{--}117\ \mu\text{m}^2$ in-plane resolution, we confirmed well-established differences in the laryngeal skeleton, such as the relatively superior extension of the cricoid cartilage (CC) lamina in infancy (i.e., prior to its developmental descent [Wilton & Hack, 2019]) and flattening of the contour of the TC laminae with age (Eckel et al., 1999; Glikson et al., 2017). We further noted increased intramuscular fat deposition with age, as well as ossification of the TC and hyaline region of the arytenoid cartilage (AC) in the 74-year-old. Each observation was corroborated by histology.

Within the vocal fold, MRI capably resolved the superficial lamina propria (SLP) from the deeper and relatively hyperintense vocal ligament (VL); the anterior macula flava (AMF) from both the anterior commissure tendon and VL; and the posterior macula flava (PMF) from the VL as well as the elastic and hyaline AC (Figure 1b). Consistent with prior reports of the infant larynx (Hartnick et al., 2005; Sato et al., 2001), the 13-month-old specimen exhibited intact AMF and PMF separated by a uniform density LP that contained no detectable VL; histology from this specimen showed an immature, partially formed ligament (Figure 1c). Volume rendering and measurement of the AMF and PMF highlighted their 3D teardrop morphology, consistently greater volume in the anterior location, and proportional volume increase during development (Video S4): 0.95 versus 0.33 μl in the 13-month-old AMF and PMF, respectively (anterior-to-posterior ratio, 2.86:1); 1.29 versus 0.47 μl in the 10-year-old AMF and PMF, respectively (anterior-to-posterior ratio, 2.72:1); 3.26 versus 1.12 μl in the 74-year-old AMF and PMF, respectively (anterior-to-posterior ratio, 2.91:1).

Next, we performed DTI to evaluate water diffusion and primary fibre orientation (Video S5). Trace maps at the level of the glottis indicated that diffusivity was highest in the LP compared to adjacent structures; directionally encoded colour maps were consistent with the known orientation of the intrinsic laryngeal muscles (Figure 2a).

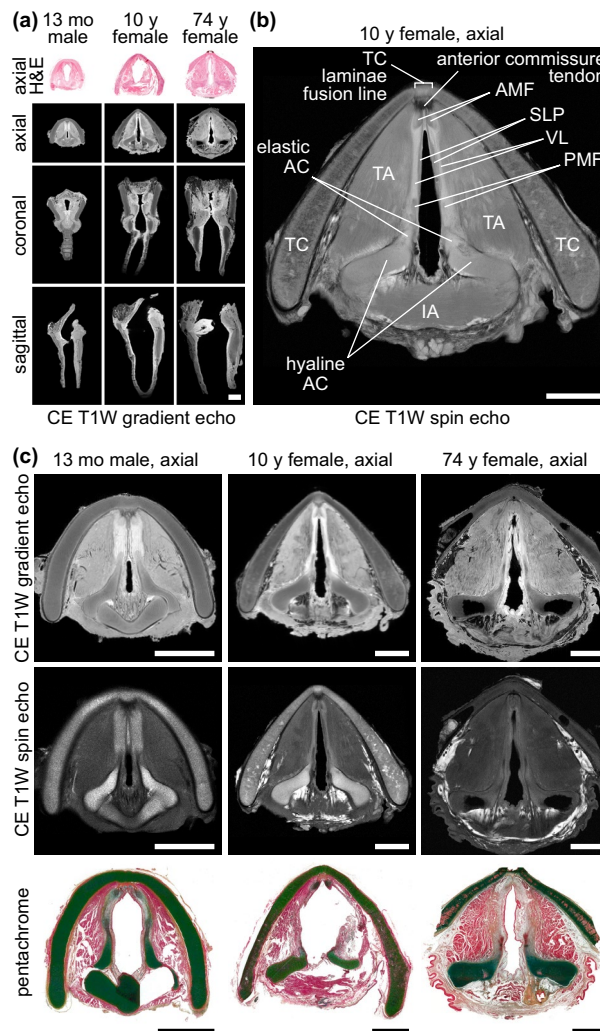


FIGURE 1 High-resolution MRI of paediatric and adult cadaveric human larynges at the glottis. (a) Orthogonal CE T1W gradient echo images showing orientation of the glottis in the axial, coronal and sagittal planes. The corresponding H&E-stained histological images are in the axial plane. Images are shown at a uniform scale to reflect relative specimen size. (b) CE T1W spin echo axial image showing resolution of vocal fold substructures in a 10-year-old female larynx. (c) CE T1W gradient echo and spin echo and corresponding pentachrome-stained histological images of a 13-month-old male, 10-year-old female and 74-year-old female larynx at the glottis in the axial plane. Note: The 13-month-old specimen exhibits a hyperintense signal artefact at the anterior glottis due to fluid trapped between the vocal folds during MRI; the 74-year-old specimen had the lateral TC laminae resected prior to imaging; the histological images exhibit moderate connective tissue shrinkage and tearing artefacts. AC, arytenoid cartilage; AMF, anterior macula flava; CE, contrast-enhanced; H&E, haematoxylin and eosin; IA, interarytenoid muscle; mo, month; MRI, magnetic resonance imaging; PMF, posterior macula flava; SLP, superficial lamina propria; T1W, T1-weighted; TA, thyroarytenoid muscle; TC, thyroid cartilage; VL, vocal ligament; y, year. Scale bars, 5 mm

Quantitative analysis of six intrinsic laryngeal muscle and two mucosal subsites showed: lower fractional anisotropy (i.e., greater isotropy) in mucosa compared to skeletal muscle, as well as higher mean

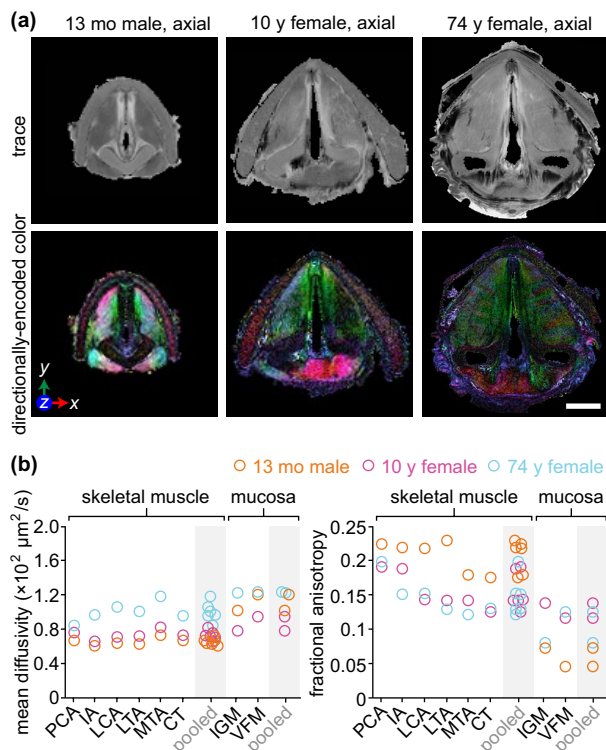


FIGURE 2 DTI of paediatric and adult cadaveric human larynges. (a) Trace and directionally encoded colour maps of a 13-month-old male, 10-year-old female and 74-year-old female larynx at the glottis in the axial plane. The trace maps show the diffusivity of water within the specimens. The directionally encoded colour maps are weighted by anisotropy and show the primary orientation of tissue fibres: green, anterior-posterior; red, medial-lateral; blue, cranial-caudal. Note: The 74-year-old specimen had the lateral thyroid cartilage laminae resected prior to imaging. (b) Mean diffusivity and fractional anisotropy of six skeletal muscle and two mucosal regions within each larynx. Measurements were obtained via manual tracing of each region of interest in the relevant DTI images from each full larynx scan. DTI, diffusion tensor imaging; IA, interarytenoid muscle; IGM, infraglottic mucosa; LCA, lateral cricoarytenoid muscle; LTA, lateral thyroarytenoid muscle; mo, month; MTA, medial thyroarytenoid muscle; PCA, posterior cricoarytenoid muscle; VFM; vocal fold mucosa; y, year. Scale bar, 5 mm

diffusivity and lower fractional anisotropy in the skeletal muscles of the older specimens (Figure 2b). We observed the greatest divergence between muscle (lower mean diffusivity, higher fractional anisotropy) and mucosal (higher mean diffusivity, lower fractional anisotropy) diffusion properties in the 13-month-old specimen.

3.2 | Characterisation of polypoid degeneration

The polypoid degeneration lesion in the 74-year-old specimen was accompanied by patchy leukoplakia on the epithelial surface (Figure 3a). The 149 μl lesion core (Video S6) exhibited hyperintensity on CE T1W imaging; the surface leukoplakia was relatively less intense (Figure 3b). On DTI, the lesion showed greater diffusivity

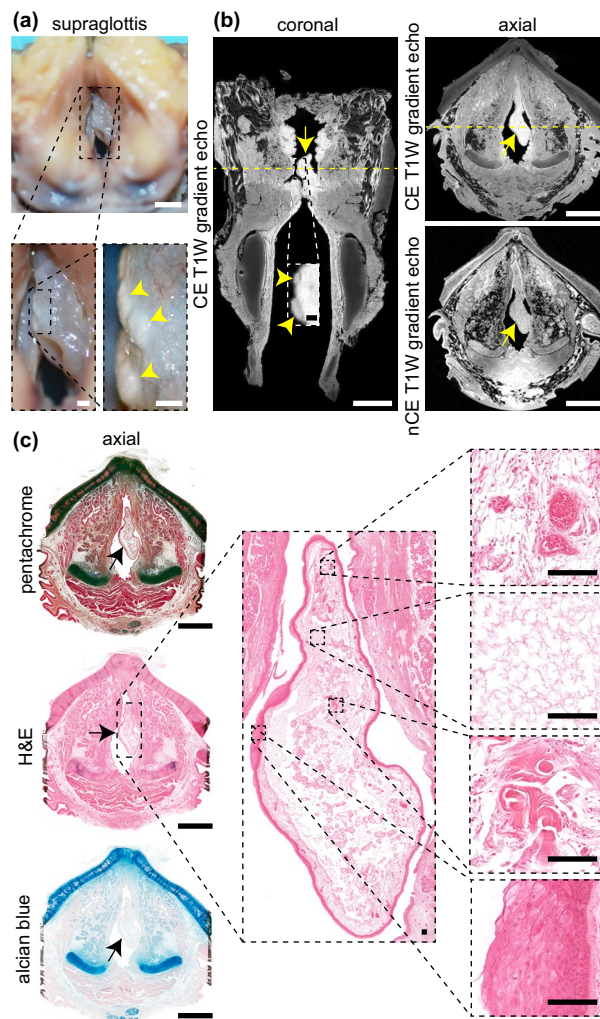


FIGURE 3 MRI and histological characterisation of polypoid degeneration. (a) Superior view of the supraglottis and vocal fold mucosae at the time of procurement from a 74-year-old female donor. Yellow arrowheads denote leukoplakia on the epithelial surface. (b) CE (coronal and axial) and nCE (axial) T1W gradient echo images showing the lesion boundary in both planes. Yellow arrows denote the lesion; yellow arrowheads denote leukoplakia. Dashed yellow lines denote the position of orthogonal views in the respective CE coronal and axial images. Note: The lateral thyroid cartilage laminae were resected prior to imaging. (c) Pentachrome-, H&E- and alcian blue-stained histological images of the lesion in the same axial view as shown on MRI. Black arrows denote the lesion. The high-magnification H&E images show (top-to-bottom): capillary wall thickening and extravascular leakage of red blood cells; an edematous lake; dense fibrin deposits; epithelial hyperparakeratosis and basement membrane thickening. CE, contrast-enhanced; H&E, haematoxylin and eosin; nCE, non-contrast-enhanced; MRI, magnetic resonance imaging; T1W, T1-weighted. Scale bars, 5 mm (whole-larynx photography, MRI and histology); 500 μm (high-magnification photography and MRI); 100 μm (high-magnification histology)

and lower fractional anisotropy than all skeletal muscle and mucosal subsites in the same specimen (Figure 7). Histology revealed: (a) capillary wall thickening and extravascular leakage of red blood cells; (b) acellular stromal regions containing edematous lakes; (c) dense

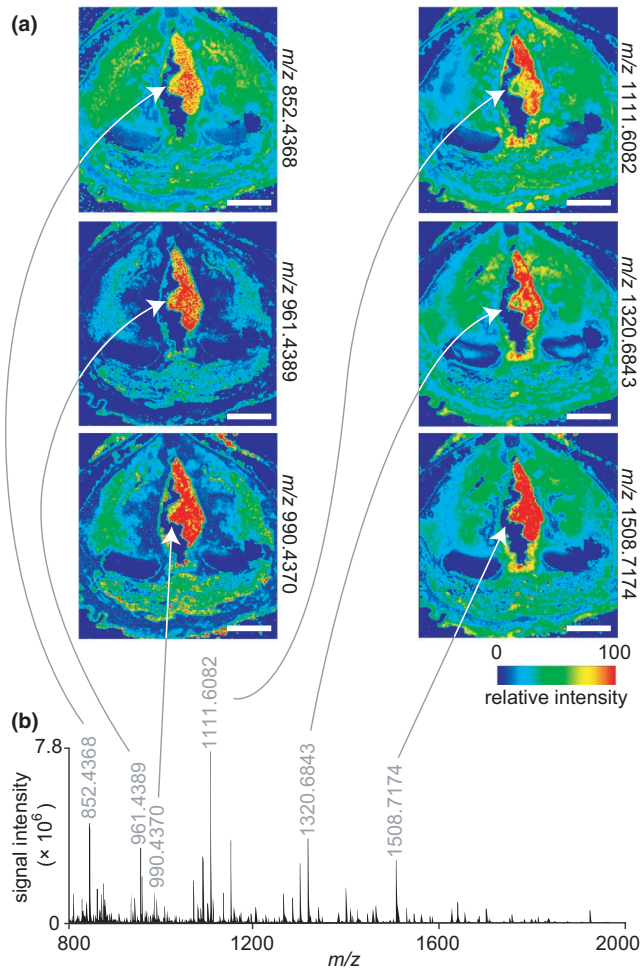


FIGURE 4 MALDI-MS imaging and proteomic analysis of polypoid degeneration. (a) Ion maps from a peptide acquisition run showing the spatial distribution of six peptides with elevated relative intensity throughout the lesion. White arrows denote the lesion. The donor was a 74-year-old female. (b) Representative mass spectrum acquired from the lesion region. The annotated peaks correspond to the ion maps in panel (a). MALDI-MS, matrix-assisted laser desorption/ionisation-mass spectrometry; m/z , mass-to-charge ratio. Scale bars, 5 mm

fibrin deposits; and (d) epithelial hyperparakeratosis with basement membrane thickening, localised to the regions that were leukoplakic on gross examination (Figure 3c). These observations are consistent with prior reports of the pathophysiology of polypoid degeneration in human patients (Dikkers & Nikkels, 1995, 1999).

Follow-up proteomic analysis using on-tissue tryptic digests and MALDI-MS imaging revealed a series of peptides with elevated intensity signatures in the lesion region compared to the adjacent mucosa (Figure 4). Mass fingerprinting of the full set of lesion-specific peptides yielded 33 putative protein assignments (Table 1), including proteins involved in interferon induction for innate immunity (interferon-induced helicase C domain-containing protein 1 [IFIH1]; E3 ubiquitin/ISG15 ligase TRIM25 [TRIM25]); epithelial keratinisation and cornification (keratin, type II cytoskeletal

1b [KRT77]; sciellin [SCEL]); cellular proliferation and growth (dual specificity protein phosphatase 4 [DUSP4]; myotubularin-related protein 6 [MTMR6]; guanine nucleotide exchange protein SMCR8 [SMCR8]; UPF0258 protein KIAA1024 [MINAR1]); and carcinogenesis (BCRA1-associated protein [BRAP]; metastasis-associated in colon cancer protein-1 [MACC1]; sulfotransferase 1A2 [SULT1A2]).

3.3 | Characterisation of mucus retention cysts

The infraglottic vocal process lesion in the 10-year-old specimen was 1.5 μl (Video S6) and exhibited a hyperintense and circumscribed core (with relatively hypointense capsule) on CE T1W imaging, a hypointense core (with relatively hyperintense capsule) on nCE T1W imaging, and a hyperintense core (with relatively hypointense capsule) on nCE T2W imaging (Figure 5a). T2W imaging additionally showed the lesion located among a chain of hyperintense structures distributed circumferentially around the posterior infraglottis, consistent with the distribution of the posterior commissure mucous glands (Nassar & Bridger, 1971). Several of these glandular structures appeared to have ducts extending to the lumen. Histologically, the lesion capsule was comprised of epithelia on both sides of a stroma (Figure 5b); the lesion core was absent, presumably lost during tissue processing. These MR and histological findings are consistent with a diagnosis of mucus retention cyst.

We identified a radiologically similar 17.3 μl lesion in the supraglottic mucosa of the 74-year-old specimen (Video S6)—presumably incidental to the polypoid degeneration finding. As in the 10-year-old specimen, this lesion exhibited a hyperintense core (with relatively hypointense capsule) on CE T1W imaging, in contrast with a hypointense core (with relatively hyperintense capsule) on nCE T1W imaging (Figure 5c). Alcian blue- and pentachrome-stained sections showed an acellular, mucin-dense lesion core surrounded by a circumferential epithelial lining; the lesion resided in an excretory duct immediately cranial to the superior aspect of the laryngeal ventricle (Figure 5d).

Given preservation of the lesion core on tissue sections from the 74-year-old specimen, we assayed its molecular signature using MALDI-MS imaging. On-tissue proteomic analysis revealed the complete absence of peptide-associated ions in the lesion core (Figure 6a), indicating relatively low protein content and supporting the likely presence of mucus. Glycan profiling detected six high-mannose and complex N-glycans within the lesion (Figure 6b,c), corroborating its positive mucin stain on histology and giving greater specificity to its glycomic make-up. These MR, histological and glycomic findings are consistent with a diagnosis of mucus retention cyst.

DTI of the two cysts showed enhanced water diffusion within both lesion cores; in both specimens, mean diffusivity was greater than that measured in all adjacent skeletal muscle and mucosal subsites (Figure 7). Fractional anisotropy in the 10-year-old specimen's cyst was lower than that in all adjacent subsites, whereas fractional anisotropy in the 74-year-old specimen's cyst was comparable to all adjacent subsites.

TABLE 1 Polypoid degeneration protein assignments, obtained by peptide mass fingerprinting. Proteins are listed in order of descending MOlecular Weight SEarch (MOWSE) score, with a lower cut-off of 75. The MOWSE score reflects the statistical confidence of the protein assignment and is defined as $-\log_{10} P$ of the assignment occurring by chance

Protein name	UniProt accession number	Gene symbol	MOWSE score	Sequence coverage (%)
Interferon-induced helicase C domain-containing protein 1	Q9BYX4	IFIH1	437	4.2
BRCA1-associated protein	Q7Z569	BRAP	300	5.1
Guanine nucleotide-binding protein G(T) subunit γ -T1	P63211	GNGT1	290	31.1
Zinc finger protein 57 homolog	Q9NU63	ZFP57	280	9.3
Heat shock protein β -1	P04792	HSPB1	270	25.9
Regulator of G-protein signalling 11	O94810	RGS11	243	4.3
α -crystallin A chain	P02489	CRYAA	227	15.6
Coiled-coil domain-containing protein 186	Q7Z3E2	CCDC186	199	6.1
Susceptibility protein NSG-x	Q9UH64	CDKN2A-DT	182	27.8
GEM-interacting protein	Q9P107	GMIP	176	4
Graves disease carrier protein	P16260	SLC25A16	172	13
Keratin, type II cytoskeletal 1b	Q7Z794	KRT77	167	8.8
Zinc finger protein 493	Q6ZR52	ZNF493	154	9.3
Dual specificity protein phosphatase 4	Q13115	DUSP4	145	5.3
Myotubularin-related protein 6	Q9Y217	MTMR6	144	11.4
Guanine nucleotide exchange protein SMCR8	Q8TEV9	SMCR8	143	4.8
Opsin-5	Q6U736	OPN5	138	5.4
Myoneurin	Q9NPC7	MYNN	138	4.6
Metastasis-associated in colon cancer protein 1	Q6ZN28	MACC1	138	5.3
UPF0258 protein KIAA1024	Q9UPX6	MINAR1	134	5.6
SRR1-like protein	Q9UH36	SRRD	134	12.4
Methionine--tRNA ligase, cytoplasmic	P56192	MARS1	126	3.4
Synaptotagmin-6	Q5T7P8	SYT6	123	6.3
Phostensin	Q6NYC8	PPP1R18	122	5.9
HLA class I histocompatibility antigen, B-58 α chain	P10319	HLA-B	120	11.3
Rho-related BTB domain-containing protein 1	O94844	RHOBTB1	118	9.1
Sciellin	O95171	SCEL	95	5.8
Seizure protein 6 homolog	Q53EL9	SEZ6	92	4.2
Fibrinogen C domain-containing protein 1	Q8N539	FIBCD1	91	4.8
Sulfotransferase 1A2	P50226	SULT1A2	81	16.6
E3 ubiquitin/ISG15 ligase TRIM25	Q14258	TRIM25	77	3.3
Protein SIX6OS1	Q8N1H7	SIX6OS1	71	7.5
PCI domain-containing protein 2	Q5JVF3	PCID2	75	9.3

4 | DISCUSSION

Using high-value paediatric and adult human larynges containing pathologies, we performed proof-of-concept imaging via two complimentary modalities: high-resolution MRI, providing nondestructive characterisation of whole-specimen microanatomy, water diffusivity and tissue fibre orientation; and MALDI-MS imaging, providing *in situ* characterisation of proteomic and glycomic signatures. Given the importance of precise assessment of subepithelial structures for clinical workup and disease surveillance, as well as for pathologic analysis of biopsied tissue, both imaging modalities

have the potential to enhance preclinical research and, eventually, clinical care.

Clinical MRI, generally performed at field strengths from 1.5 to 3.0 T, has shown value in assessing laryngoplastic implants (Ford et al., 1995), vascular anomalies (Guneyli et al., 2014) and cancer invasion (Agnello et al., 2017; Maroldi et al., 2014; Preda et al., 2017); moreover, it has been endorsed for laryngeal workup in infants and children due to the absence of ionising radiation (Elders et al., 2019). DTI is also used clinically and has shown utility in discriminating neoplastic laryngeal tissue from adjacent oedema (Elders et al., 2019; Maroldi et al., 2014). Here, using an *ex vivo* setup at 4.7 T,

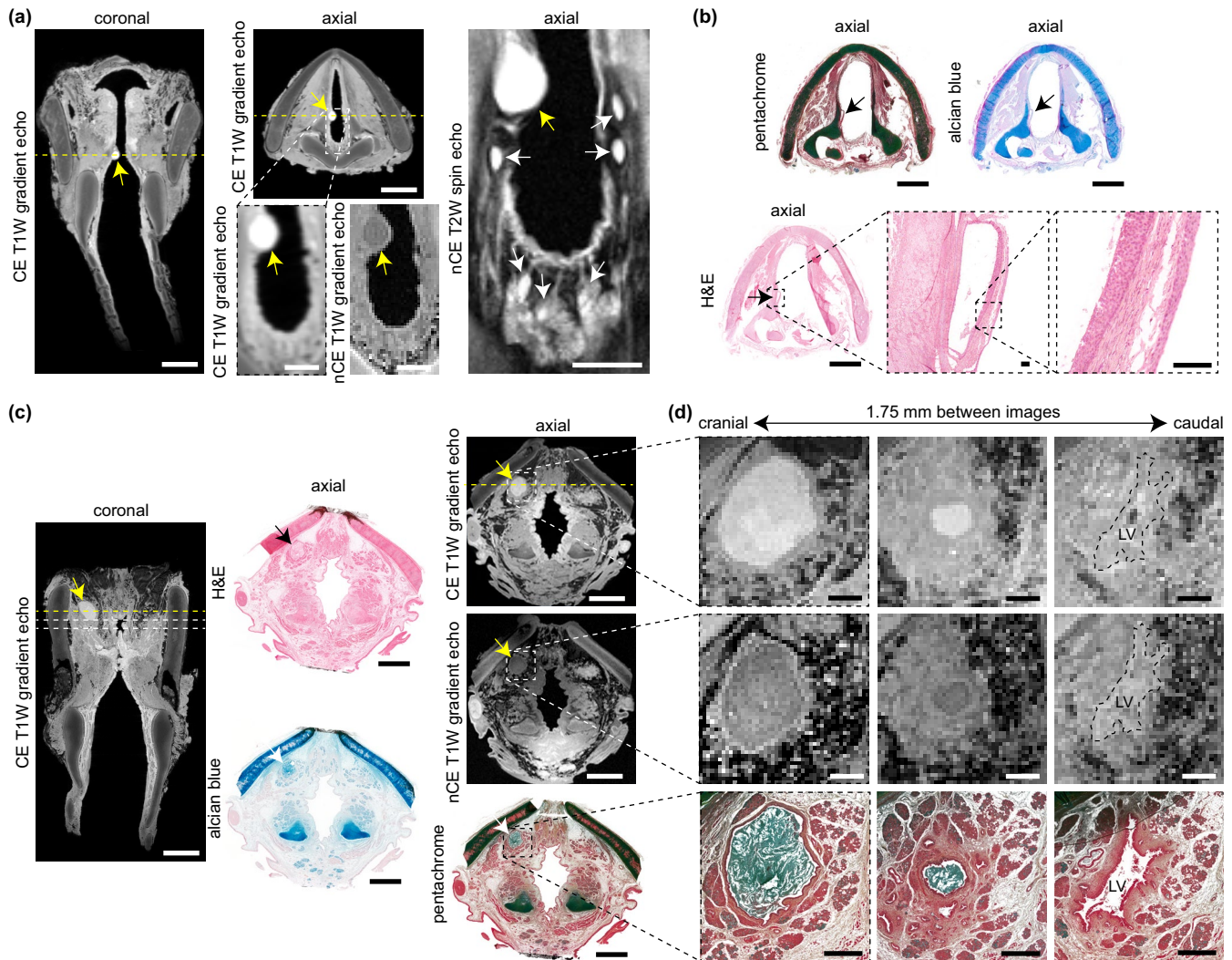


FIGURE 5 MRI and histological characterisation of mucus retention cysts. (a) CE T1W gradient echo coronal and axial images, alongside high-magnification CE T1W gradient echo, nCE T1W gradient echo, and nCE T2W spin echo axial images, showing an infraglottic lesion in a 10-year-old female. Yellow arrows denote the lesion; white arrows denote adjacent mucous glands within the posterior infraglottis. Dashed yellow lines denote the position of orthogonal views in the respective CE coronal and axial images. (b) Pentachrome-, alcian blue- and H&E-stained histological images of the lesion in the same axial view as shown on MRI. Black arrows denote the lesion. The high-magnification H&E images show a cyst wall comprised of stroma and both internal and external epithelia; the cyst contents are absent. Note: The images exhibit moderate connective tissue shrinkage and tearing artefacts. (c) CE (coronal and axial) and nCE (axial) T1W gradient echo images showing a supraglottic lesion in a 74-year-old female. The corresponding H&E-, alcian blue, and pentachrome- stained images show the same axial view as seen on MRI. Yellow, black and white arrows denote the lesion. The dashed yellow lines denote the position of orthogonal views in the respective CE coronal and axial images; additionally, the dashed lines in the coronal image denote the positions of the high-magnification axial images in panel (d). (d) Serial CE and nCE T1W gradient echo and corresponding pentachrome-stained histological images of the lesion at high magnification in the axial plane. The images are 1.75 mm apart and show a decrease in lesion size followed by entry to the LV in the cranial-to-caudal direction. The histology shows a circumferential epithelial lining and mucin-dense lesion core (blue-green signal). Note: The 74-year-old specimen had the lateral thyroid cartilage laminae resected prior to imaging; the histologic images exhibit moderate connective tissue shrinkage and tearing artefacts. CE, contrast-enhanced; H&E, haematoxylin and eosin; LV, laryngeal ventricle; MRI, magnetic resonance imaging; nCE, non-contrast-enhanced; T1W, T1-weighted; T2W, T2-weighted. Scale bars, 5 mm (whole-larynx MRI and histology); 1 mm (high-magnification MRI and histology in panel [d]); 100 μ m (high-magnification histology in panel [b])

immersion Gd CE, optimised acquisition sequences and extended acquisition times, we microimaged vocal fold substructures that—to our knowledge—have not been previously reported radiographically. We resolved laryngeal pathologies with delineation of polypoid degeneration from patchy leukoplakia on the epithelial surface, as

well as cyst lesion cores from their capsules; further, we quantified diffusion features with direct applicability to laryngeal tissue fibre organisation and disease presentation.

Despite these advances, care is required when interpreting our findings and considering future clinical translation. In addition to

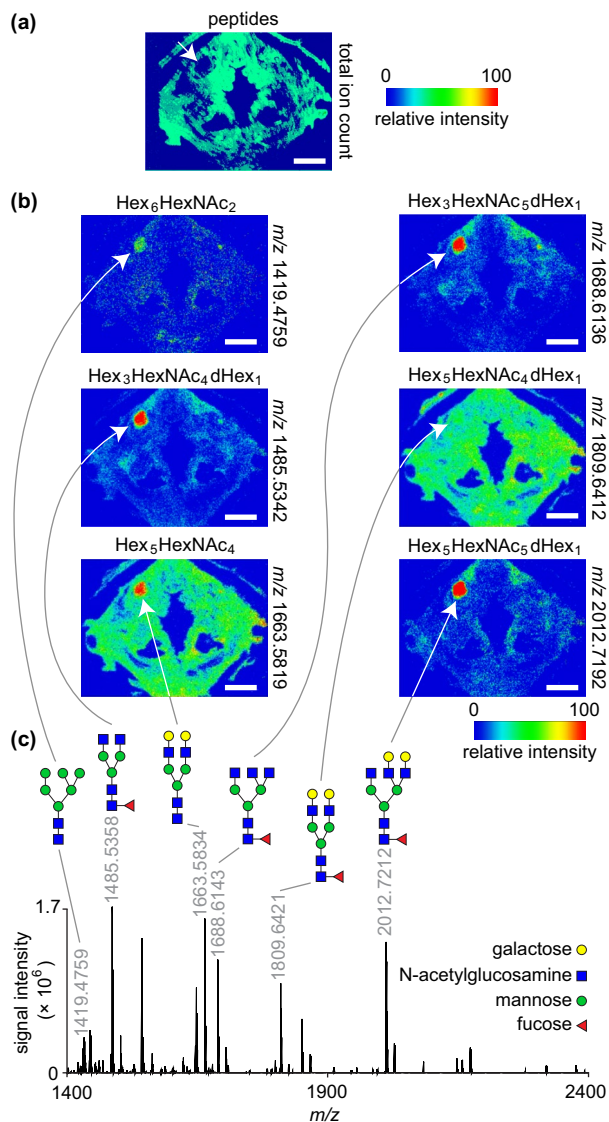


FIGURE 6 MALDI-MS imaging and glycomic analysis of a mucus retention cyst. (a) Total ion count map from a peptide acquisition run showing the spatial distribution of summed peptide intensities. The white arrow denotes the lesion and shows no peptide signal in this region. The donor was a 74-year-old female. (b) Ion maps from a glycan acquisition run showing the spatial distribution of six N-glycans identified throughout the lesion. White arrows denote the lesion. (c) Representative mass spectrum acquired from the lesion region. The annotated peaks correspond to the ion maps in panel (b). N-glycan structures are depicted using the Symbol Nomenclature for Glycans (SNFG) format; note that the identified glycans are all in the sodiated adduct form as $[M + Na]^+$. MALDI-MS, matrix-assisted laser desorption/ionisation-mass spectrometry; m/z , mass-to-charge ratio. Scale bars, 5 mm

the possibility of postmortem autolysis, tissue fixation with PFA, prolonged immersion in Gd for CE imaging, and later washout of PFA and Gd for DTI, likely yields different tissue contrast features than are seen during *in vivo* imaging of human patients, for whom Gd CE is delivered intravenously. For example, cysts classically exhibit hyperintensity on T2W imaging, alongside relative hypointensity

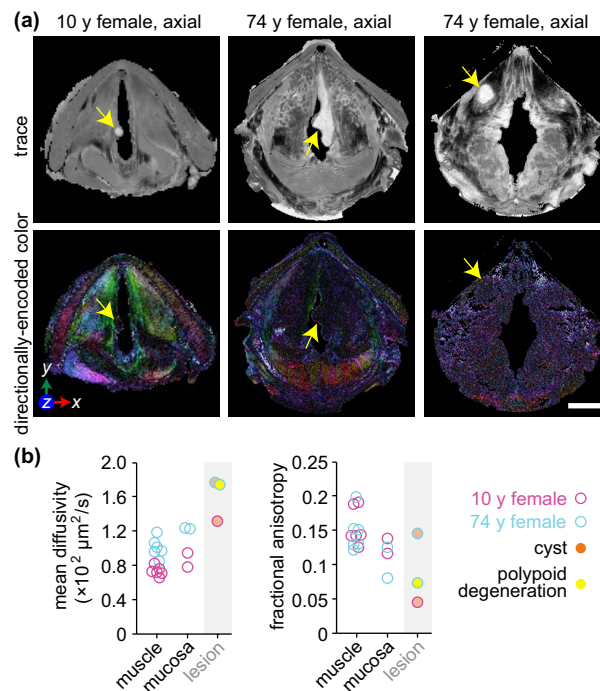


FIGURE 7 DTI of mucus retention cysts and polypoid degeneration. (a) Trace and directionally encoded colour maps of an infraglottic mucus retention cyst in a 10-year-old female, polypoid degeneration in a 74-year-old female and supraglottic mucus retention cyst in the same 74-year-old female. The trace maps show the diffusivity of water within the specimens. The directionally encoded colour maps are weighted by anisotropy and show the primary orientation of tissue fibres: green, anterior-posterior; red, medial-lateral; blue, cranial-caudal. Note: The 74-year-old specimen had the lateral thyroid cartilage laminae resected prior to imaging. (b) Mean diffusivity and fractional anisotropy of the three lesions compared to skeletal muscle and mucosa in the same larynges. The muscle and mucosal regions are those shown in Figure 2b. Measurements were obtained via manual tracing of each region of interest in the relevant DTI images from each full larynx scan. DTI, diffusion tensor imaging; y, year. Scale bar, 5 mm

on T1W imaging that is not subject to CE (Wu & Hochman, 2009); however, we observed hyperintensity of both cyst lesion cores on CE T1W imaging, suggesting that the Gd agent permeated the cyst during the 10-day immersion period. Similarly, despite our use of a prolonged washout protocol, incomplete removal of PFA from any tissue region could have influenced our DTI data via the known impact of aldehyde fixatives on water diffusivity within tissue (Shepherd et al., 2009).

Practical implementation of high-resolution laryngeal MRI in human patients also requires increased field strengths, improved signal-to-noise ratios and shorter acquisition times. Recent progress has been made using phased-array surface coils applied to the neck (Maroldi et al., 2014; Preda et al., 2017); further improvements are expected with ongoing technology development and wider availability of high-field-strength instruments: *in vivo* MRI has been reported in humans at 9.4 T (Pohmann et al., 2016) and even higher-resolution

in vivo MRI is feasible in rodents at 16.4 and 21.1 T (Schepkin et al., 2010; Shajan et al., 2012; Ullmann et al., 2013, 2014). Additional considerations for optimising *in vivo* laryngeal MRI include the use of behavioural, acquisition and analytical techniques to compensate for motion artefacts associated with carotid artery pulsation, breathing and swallowing (Ehman et al., 1984; Maroldi et al., 2014; Nygren et al., 2016).

MALDI-MS imaging generates ion density maps of biomolecules *in situ* by acquiring mass spectra on a predefined grid, providing detailed molecular characterisation within microanatomic context (Caprioli et al., 1997; Stauber et al., 2010; Zhang et al., 2020). Due to ongoing improvements in sensitivity and spatial resolution, MS imaging is increasingly relevant to clinical imaging and pathological readout. For example, the recent development of ambient ionisation techniques has extended the application of MS imaging to determining tumour margins in the operating room (Calligaris et al., 2015; Eberlin et al., 2016). Here, we observed proteomic and glycomic lesion signatures that corroborated our MRI and histology data and align with current pathophysiological understanding of these disorders (Dijkers & Nikkels, 1995, 1999; Duflo et al., 2006; Gipson et al., 1995; Gray et al., 1995; Remacle et al., 1996; Thibeault et al., 2002; van der Velden et al., 1996). In the case of the polypoid degeneration lesion with surface leukoplakia, the proteomic data were indicative of epithelial hyperkeratosis (the pathological phenotype underlying clinical leukoplakia in normally non-keratinised squamous epithelial cells), cellular proliferation and growth (consistent with both the inflamed stroma and its hyperplastic epithelium) and carcinogenesis (not typically associated with polypoid degeneration but consistent with hyperkeratotic epithelial cells exhibiting premalignant features). In the case of the mucus retention cyst—which is defined by its ductal location and mucin-rich content—the glycomic data revealed specific glycan species, offering new insight into the nature of mucin glycosylation within secreted (and, in this case, retained) laryngeal mucus. As observations based on single lesion specimens, however, these data should be interpreted cautiously and primarily used to direct further validation, hypothesis generation and mechanistic work.

In summary, our data show the potential of high-resolution MR and MALDI-MS imaging techniques for characterising normal and pathological human laryngeal tissues, pursuing biomarker discovery and supporting mechanistic studies. With ongoing development, next-generation instruments and translational methodologies may assist clinicians and surgeons as they assess ambiguous subepithelial tissue changes, evaluate clinical biopsies and surgical margins, and make treatment decisions.

ACKNOWLEDGEMENTS

This work was supported by grants R01 DC004428 (NVW), R01 DC010777 (NVW) and R21 DC017836 (XS and NVW) from the National Institute on Deafness and Other Communication Disorders; grant R01 DK071801 (LL) from the National Institute on Diabetes and Digestive and Kidney Diseases; grant R56 MH110215 (LL) from the National Institute of Mental Health; grant U01 CA231081 (LL) from the National Cancer Institute; and the University of Wisconsin

Head and Neck Cancer SPORE, supported by grant P50 DE026787 from the National Institute of Dental and Craniofacial Research. The MRI instrument is housed in the University of Wisconsin Small Animal Imaging and Radiotherapy facility, supported by grant P30 CA014520 from the National Cancer Institute; the MALDI Orbitrap instrument was purchased with support from shared instrument grant S10 RR029531 from the National Center for Research Resources. The authors have no other funding, financial relationships or conflicts of interest to disclose. We gratefully acknowledge Erin Brooks and Jodi Corbit (Department of Pathology, University of Wisconsin-Madison) for larynx procurement, Beth Rauch (Department of Medical Physics, University of Wisconsin-Madison) for assistance with MRI, Toshi Kinoshita (Department of Pathology, University of Wisconsin-Madison) for assistance with histology and Karen Lynch (Department of Surgery, University of Wisconsin-Madison) for assistance with video editing.

AUTHOR CONTRIBUTIONS

AOK, IJR and NVW designed the study; AOK, YK and GO dissected and processed the larynges; IJR collected MRI data; AOK, IJR and NVW analysed MRI data; EBH collected and analysed DTI data; NVW analysed histological data; HZ and YS collected and analysed MALDI-MS imaging data with guidance from XS and LL; XS conducted peptide mass fingerprinting; AOK and NVW wrote the manuscript; all authors reviewed and approved the final version.

DATA AVAILABILITY STATEMENT

Serial MRI (CE T1W gradient echo) and DTI slices are available as Supporting Information. The raw MALDI-MS imaging data are publicly available on the METASPACE platform via dataset link https://metaspace2020.eu/project/2021_aok. Additional raw data supporting the findings of this study are available from the corresponding author upon reasonable request.

ORCID

Ayami Ohno Kishimoto  <https://orcid.org/0000-0001-5071-6515>
 Yo Kishimoto  <https://orcid.org/0000-0002-3583-0165>
 Xudong Shi  <https://orcid.org/0000-0001-6469-3481>
 Elizabeth B. Hutchinson  <https://orcid.org/0000-0002-3374-5469>
 Hua Zhang  <https://orcid.org/0000-0003-2875-7243>
 Yatao Shi  <https://orcid.org/0000-0002-8240-3035>
 Lingjun Li  <https://orcid.org/0000-0003-0056-3869>
 Nathan V. Welham  <https://orcid.org/0000-0003-3484-3455>
 Ian J. Rowland  <https://orcid.org/0000-0003-2282-7765>

REFERENCES

- Agnello, F., Cupido, F., Sparacia, G., Midiri, F., Miroddi, M., Grassedonio, E. et al. (2017) Computerised tomography and magnetic resonance imaging of laryngeal squamous cell carcinoma: A practical approach. *The Neuroradiology Journal*, 30, 197–204.
- Armstrong, W.B., Ridgway, J.M., Vokes, D.E., Guo, S., Perez, J., Jackson, R.P. et al. (2006) Optical coherence tomography of laryngeal cancer. *Laryngoscope*, 116, 1107–1113.

- Burns, J.A., Kim, K.H., deBoer, J.F., Anderson, R.R. & Zeitels, S.M. (2011) Polarization-sensitive optical coherence tomography imaging of benign and malignant laryngeal lesions: An *in vivo* study. *Otolaryngology - Head and Neck Surgery*, 145, 91–99.
- Burns, J.A., Zeitels, S.M., Anderson, R.R., Kobler, J.B., Pierce, M.C. & de Boer, J.F. (2005) Imaging the mucosa of the human vocal fold with optical coherence tomography. *Annals of Otolaryngology, Rhinology, and Laryngology*, 114, 671–676.
- Calligaris, D., Feldman, D.R., Norton, I., Brastianos, P.K., Dunn, I.F., Santagata, S. et al. (2015) Molecular typing of meningiomas by desorption electrospray ionization mass spectrometry imaging for surgical decision-making. *International Journal of Mass Spectrometry*, 377, 690–698.
- Caprioli, R.M., Farmer, T.B. & Gile, J. (1997) Molecular imaging of biological samples: Localization of peptides and proteins using MALDI-TOF MS. *Analytical Chemistry*, 69, 4751–4760.
- Damerell, D., Ceroni, A., Maass, K., Ranzinger, R., Dell, A. & Haslam, S.M. (2012) The GlycanBuilder and GlycoWorkbench glycoinformatics tools: Updates and new developments. *Biological Chemistry*, 393, 1357–1362.
- Dikkers, F.G. & Nikkels, P.G. (1995) Benign lesions of the vocal folds: Histopathology and phonotrauma. *Annals of Otolaryngology, Rhinology, and Laryngology*, 104, 698–703.
- Dikkers, F.G. & Nikkels, P.G. (1999) Lamina propria of the mucosa of benign lesions of the vocal folds. *Laryngoscope*, 109, 1684–1689.
- Duflo, S.M., Thibeault, S.L., Li, W., Smith, M.E., Schade, G. & Hess, M.M. (2006) Differential gene expression profiling of vocal fold polyps and Reinke's edema by complementary DNA microarray. *Annals of Otolaryngology, Rhinology, and Laryngology*, 115, 703–714.
- Eberlin, L.S., Margulis, K., Planell-Mendez, I., Zare, R.N., Tibshirani, R., Longacre, T.A. et al. (2016) Pancreatic cancer surgical resection margins: Molecular assessment by mass spectrometry imaging. *PLoS Medicine*, 13, e1002108.
- Eckel, H.E., Sprinzl, G.M., Koebke, J., Pototschnig, C., Sittel, C. & Stennert, E. (1999) Morphology of the human larynx during the first five years of life studied on whole organ serial sections. *Annals of Otolaryngology, Rhinology, and Laryngology*, 108, 232–238.
- Ehman, R.I., McNamara, M.T., Pallack, M., Hricak, H. & Higgins, C.B. (1984) Magnetic resonance imaging with respiratory gating: Techniques and advantages. *American Journal of Roentgenology*, 143, 1175–1182.
- Elders, B.B.L.J., Hermelijn, S.M., Tiddens, H.A.W.M., Pullens, B., Wielopolski, P.A. & Ciet, P. (2019) Magnetic resonance imaging of the larynx in the pediatric population: A systematic review. *Pediatric Pulmonology*, 54, 478–486.
- Ford, C.N., Unger, J.M., Zundel, R.S. & Bless, D.M. (1995) Magnetic resonance imaging (MRI) assessment of vocal fold medialization surgery. *Laryngoscope*, 105, 498–504.
- Gipson, I.K., Spurr-Michaud, S.J., Tisdale, A.S., Kublin, C., Cintron, C. & Keutmann, H. (1995) Stratified squamous epithelia produce mucin-like glycoproteins. *Tissue and Cell*, 27, 397–404.
- Glikson, E., Sagiv, D., Eyal, A., Wolf, M. & Primov-Fever, A. (2017) The anatomical evolution of the thyroid cartilage from childhood to adulthood: A computed tomography evaluation. *Laryngoscope*, 127, E354–E358.
- Gray, S.D., Hammond, E. & Hanson, D.F. (1995) Benign pathologic responses of the larynx. *Annals of Otolaryngology, Rhinology, and Laryngology*, 104, 13–18.
- Guneyli, S., Ceylan, N., Bayraktaroglu, S., Acar, T. & Savas, R. (2014) Imaging findings of vascular lesions in the head and neck. *Diagnostic and Interventional Radiology*, 20, 432–437.
- Hartnick, C.J., Rehbar, R. & Prasad, V. (2005) Development and maturation of the pediatric human vocal fold lamina propria. *Laryngoscope*, 115, 4–15.
- Herrera, V.L.M., Viereck, J.C., Lopez-Guerra, G., Kumai, Y., Kobler, J., Karajanagi, S. et al. (2009) 11.7 Tesla magnetic resonance microimaging of laryngeal tissue architecture. *Laryngoscope*, 119, 2187–2194.
- Huang, C.-C., Sun, L., Dailey, S.H., Wang, S.-H. & Shung, K.K. (2007) High frequency ultrasonic characterization of human vocal fold tissue. *Journal of the Acoustical Society of America*, 122, 1827–1832.
- Irfanoglu, M.O., Nayak, A., Jenkins, J. & Pierpaoli, C. (2017) TORTOISE v3: Improvements and new features of the NIH diffusion MRI processing pipeline. In: Proceedings of the 25th Annual Meeting and Exhibition of the International Society of Magnetic Resonance in Medicine. Honolulu, HI, USA, April 22–27, abstract 3540. <https://cds.ismrm.org/protected/17MPProceedings/>
- Jenkinson, M., Beckmann, C.F., Behrens, T.E.J., Woolrich, M.W. & Smith, S.M. (2012) FSL. *NeuroImage*, 62, 782–790.
- Jungheim, M., Donner, S., Bleeker, S., Ripken, T., Krueger, A. & Ptok, M. (2016) Effect of saline inhalation on vocal fold epithelial morphology evaluated by optical coherence tomography. *Laryngoscope*, 126, E332–E336.
- King, R.E., Steed, K., Rivera, A.E., Wisco, J.J. & Thibeault, S.L. (2018) Magnetic resonance imaging quantification of dehydration and rehydration in vocal fold tissue layers. *PLoS One*, 13, e0208763.
- Kishimoto, A.O., Kishimoto, Y.O., Young, D.L., Zhang, J., Rowland, I.J. & Welham, N.V. (2016) High- and ultrahigh-field magnetic resonance imaging of naïve, injured and scarred vocal fold mucosae in rats. *Disease Models & Mechanisms*, 9, 1397–1403.
- Klein, A.M., Pierce, M.C., Zeitels, S.M., Anderson, R.R., Kobler, J.B., Shishkov, M. et al. (2006) Imaging the human vocal folds *in vivo* with optical coherence tomography: A preliminary experience. *Annals of Otolaryngology, Rhinology, and Laryngology*, 115, 277–284.
- Kolosova, K., Gao, Q., Bouhabel, S., Kost, K.M. & Wang, H. (2020) Characterizing vocal fold injury recovery in a rabbit model with three-dimensional virtual histology. *Laryngoscope*. Epub ahead of print, August 18. <https://doi.org/10.1002/lary.29028>
- Le Bihan, D., Mangin, J.-F., Poupon, C., Clark, C.A., Pappata, S., Molko, N. et al. (2001) Diffusion tensor imaging: Concepts and applications. *Journal of Magnetic Resonance Imaging*, 13, 534–546.
- Maroldi, R., Ravanelli, M. & Farina, D. (2014) Magnetic resonance for laryngeal cancer. *Current Opinion in Otolaryngology & Head and Neck Surgery*, 22, 131–139.
- Maturo, S., Benboujja, F., Boudoux, C. & Hartnick, C. (2012) Quantitative distinction of unique vocal fold subepithelial architectures using optical coherence tomography. *Annals of Otolaryngology, Rhinology, and Laryngology*, 121, 754–760.
- Nassar, V.H. & Bridger, G.P. (1971) Topography of the laryngeal mucous glands. *Archives of Otolaryngology*, 94, 490–498.
- Neelamegham, S., Aoki-Kinoshita, K., Bolton, E., Frank, M., Lisacek, F., Lütke, T. et al. (2019) Updates to the symbol nomenclature for glycans guidelines. *Glycobiology*, 29, 620–624.
- Nygren, U., Isberg, B., Arver, S., Hertegård, S., Södersten, M. & Nordenskjöld, A. (2016) Magnetic resonance imaging of the vocal folds in women with congenital adrenal hyperplasia and virilized voices. *Journal of Speech, Language, and Hearing Research*, 59, 713–721.
- Oleson, S., Cox, A., Liu, Z. et al. (2020) *In vivo* magnetic resonance imaging of the rat vocal folds after systemic dehydration and rehydration. *Journal of Speech, Language, and Hearing Research*, 63, 135–142.
- Oleson, S., Lu, K.-H., Liu, Z., Durkes, A.C. & Sivasankar, M.P. (2018) Proton density-weighted laryngeal magnetic resonance imaging in systemically dehydrated rats. *Laryngoscope*, 128, E222–E227.
- Pajevic, S. & Pierpaoli, C. (1999) Color schemes to represent the orientation of anisotropic tissues from diffusion tensor data: Application to white matter fiber tract mapping in the human brain. *Magnetic Resonance in Medicine*, 42, 526–540.
- Pappin, D.J., Hojrup, P. & Bleasby, A.J. (1993) Rapid identification of proteins by peptide-mass fingerprinting. *Current Biology*, 3, 327–332.
- Perkins, D.N., Pappin, D.J.C., Creasy, D.M. & Cottrell, J.S. (1999) Probability-based protein identification by searching sequence databases using mass spectrometry data. *Electrophoresis*, 20, 3551–3567.

- Pohmann, R., Speck, O. & Scheffler, K. (2016) Signal-to-noise ratio and MR tissue parameters in human brain imaging at 3, 7, and 9.4 tesla using current receive coil arrays. *Magnetic Resonance in Medicine*, 75, 801–809.
- Preda, L., Conte, G., Bonello, L., Giannitto, C., Tagliabue, E., Raimondi, S. et al. (2017) Diagnostic accuracy of surface coil MRI in assessing cartilaginous invasion in laryngeal tumours: Do we need contrast-agent administration? *European Radiology*, 27, 4690–4698.
- Remacle, M., Degols, J.C. & Delos, M. (1996) Exudative lesions of Reinke's space. An anatomopathological correlation. *Acta Oto-Rhino-Laryngologica Belgica*, 50, 253–264.
- Rosen, C.A. & Murry, T. (2000) Diagnostic laryngeal endoscopy. *Otolaryngologic Clinics of North America*, 33, 751–758.
- Sato, K., Hirano, M. & Nakashima, T. (2001) Fine structure of the human newborn and infant vocal fold mucosae. *Annals of Otolaryngology, and Laryngology*, 110, 417–424.
- Schepkin, V.D., Brey, W.W., Gor'kov, P.L. & Grant, S.C. (2010) Initial *in vivo* rodent sodium and proton MR imaging at 21.1 T. *Magnetic Resonance Imaging*, 28, 400–407.
- Schneider, C.A., Rasband, W.S. & Eliceiri, K.W. (2012) NIH Image to ImageJ: 25 years of image analysis. *Nature Methods*, 9, 671–675.
- Shajan, G., Hoffmann, J., Balla, D.Z., Deelchand, D.K., Scheffler, K. & Pohmann, R. (2012) Rat brain MRI at 16.4 T using a capacitively tunable patch antenna in combination with a receive array. *NMR in Biomedicine*, 25, 1170–1176.
- Shepherd, T.M., Thelwall, P.E., Stanisz, G.J. & Blackband, S.J. (2009) Aldehyde fixative solutions alter the water relaxation and diffusion properties of nervous tissue. *Magnetic Resonance in Medicine*, 62, 26–34.
- Stauber, J., MacAleese, L., Franck, J., Claude, E., Snel, M., Kaletas, B.K. et al. (2010) On-tissue protein identification and imaging by MALDI-ion mobility mass spectrometry. *Journal of the American Society for Mass Spectrometry*, 21, 338–347.
- Sulica, L. (2013) Laryngoscopy, stroboscopy and other tools for the evaluation of voice disorders. *Otolaryngologic Clinics of North America*, 46, 21–30.
- Tamura, E., Kitahara, S. & Kohno, N. (2001) Clinical assessment of intralaryngeal ultrasonography. *Laryngoscope*, 111, 1767–1770.
- Tamura, E., Kitahara, S. & Kohno, N. (2002) Intralaryngeal application of a miniaturized ultrasonic probe. *Acta Oto-Laryngologica*, 122, 92–95.
- Thibeault, S.L., Ford, C.N., Gray, S.D., Smith, M.E., Li, W. & Davis, R.K. (2002) Genotypic and phenotypic expression of vocal fold polyps and Reinke's edema: A preliminary study. *Annals of Otolaryngology, and Laryngology*, 111, 302–309.
- Ullmann, J.F.P., Watson, C., Janke, A.L., Kurniawan, N.D., Paxinos, G. & Reutens, D.C. (2014) An MRI atlas of the mouse basal ganglia. *Brain Structure and Function*, 219, 1343–1353.
- Ullmann, J.F.P., Watson, C., Janke, A.L., Kurniawan, N.D. & Reutens, D.C. (2013) A segmentation protocol and MRI atlas of the C57BL/6J mouse neocortex. *NeuroImage*, 78, 196–203.
- Van Der Velden, L.-A., Schaafsma, H.E., Manni, J.J., Link, M., Ruiter, D.J., Ramaekers, F.C.S. et al. (1996) Cytokeratin and vimentin expression in normal epithelium and benign lesions of the vocal cords. *Acta Oto-Laryngologica* 116, 325–331.
- Walsh, C.J., Heaton, J.T., Kobler, J.B., Szabo, T.L. & Zeitels, S.M. (2008) Imaging of the calf vocal fold with high-frequency ultrasound. *Laryngoscope*, 118, 1894–1899.
- Wilton, N. & Hack, H. (2019) Developmental anatomy of the airway. *Anaesthesia & Intensive Care Medicine*, 20, 29–34.
- Wittekindt, C., Sittel, C., Greiss, J., Drebber, U., Edmund Eckel, H. & Florian Preuss, S. (2008) Mapping of Ki-67 protein distribution on whole organ serial sections of the larynx. *Acta Oto-Laryngologica*, 128, 207–212.
- Wittekindt, C., Sittel, C., Kvasnicka, H.M. & Eckel, H.E. (2006) Immunohistochemistry of whole-organ sections of advanced human laryngeal cancer. *European Archives of Oto-Rhino-Laryngology*, 263, 741–746.
- Wong, B.J.F., Jackson, R.P., Guo, S., Ridgway, J.M., Mahmood, U., Su, J. et al. (2005) *In vivo* optical coherence tomography of the human larynx: Normative and benign pathology in 82 patients. *Laryngoscope*, 115, 1904–1911.
- Wu, J.S. & Hochman, M.G. (2009) Soft-tissue tumors and tumorlike lesions: A systematic imaging approach. *Radiology*, 253, 297–316.
- Zhang, H., Shi, X., Vu, N.Q., Li, G., Li, Z., Shi, Y. et al. (2020) On-tissue derivatization with Girard's reagent P enhances N-glycan signals for formalin-fixed paraffin-embedded tissue sections in MALDI mass spectrometry imaging. *Analytical Chemistry*, 92, 13361–13368.

SUPPORTING INFORMATION

Additional supporting information may be found online in the Supporting Information section.

How to cite this article: Kishimoto AO, Kishimoto Y, Shi X, et al. High-resolution magnetic resonance and mass spectrometry imaging of the human larynx. *J Anat.* 2021;239:545–556. <https://doi.org/10.1111/joa.13451>